Oxygen Transport Ceramic Membranes

Quarterly Report

May 2005 – June 2005

Principal Authors:

Prof. S. Bandopadhyay

Dr. T. Nithyanantham

Issued: August 2005

DOE Award # DE-FC26-99FT40054

University of Alaska Fairbanks
Fairbanks, AK 99775

Contributing sub contractors:

1. **X.-D Zhou, Y-W. Sin and H. U. Anderson,** Materials Research Center, University of Missouri-Rolla, Rolla, MO 65401
2. **Prof. Alan Jacobson and Prof. C.A. Mims;** University of Houston/University of Toronto

DISCLAIMER

ABSTRACT

The present quarterly report describes some of the investigations on the structural properties of dense OTM bars provided by Praxair and studies on newer composition of Ti doped LSF.

In the previous research, the reference point of oxygen occupancy was determined and verified. In the current research, the oxygen occupancy was investigated at 1200^{o}C as a function of oxygen activity and compared with that at 1000^{o}C. The cause of bumps at about 200^{o}C was also investigated by using different heating and cooling rates during TGA.

The fracture toughness of LSFT and dual phase membranes at room temperature is an important mechanical property. Vicker's indentation method was used to evaluate this toughness. Through this technique, a K_{Ic} (Mode-I Fracture Toughness) value is attained by means of semi-empirical correlations between the indentation load and the length of the cracks emanating from the corresponding Vickers indentation impression. In the present investigation, crack propagation behavior was extensively analyzed in order to understand the strengthening mechanisms involved in the non-transforming La based ceramic composites. Cracks were generated using Vicker's indenter and used to identify and evaluate the toughening mechanisms involved.

Preliminary results of an electron microscopy study of the origin of the slow kinetics on reduction of ferrites have been obtained. The slow kinetics appear to be related to a non-equilibrium reduction pathway that initially results in the formation of iron particles. At long times, equilibrium can be reestablished with recovery of the perovskite phase.

Modeling of the isotopic transients on operating membranes (LSCrF-2828 at 900°C) and a "frozen" isotope profile have been analyzed in conjunction with a 1-D model to reveal the gradient in oxygen diffusivity through the membrane under conditions of high chemical gradients.

TABLE OF CONTENTS

LIST OF GRAPHICAL MATERIALS

INTRODUCTION

Conversion of natural gas to liquid fuels and chemicals is a major goal for the Nation as it enters the 21st Century. Technically robust and economically viable processes are needed to capture the value of the vast reserves of natural gas on Alaska's North Slope, and wean the Nation from dependence on foreign petroleum sources. Technologies that are emerging to fulfill this need are all based syngas as an intermediate. Syngas (a mixture of hydrogen and carbon monoxide) is a fundamental building block from which chemicals and fuels can be derived. Lower cost syngas translates directly into more cost-competitive fuels and chemicals.

The currently practiced commercial technology for making syngas is either steam methane reforming (SMR) or a two-step process involving cryogenic oxygen separation followed by natural gas partial oxidation (POX). These high-energy, capital-intensive processes do not always produce syngas at a cost that makes its derivatives competitive with current petroleum-based fuels and chemicals.

In the mid 80's BP invented a radically new technology concept that will have a major economic and energy efficiency impact on the conversion of natural gas to liquid fuels, hydrogen, and chemicals.[1] This technology, called Electropox, integrates oxygen separation with the oxidation and steam reforming of natural gas into a single process to produce syngas with an economic advantage of 30 to 50 percent over conventional technologies.[2]

The Electropox process uses novel and proprietary solid metal oxide ceramic oxygen transport membranes [OTMs], which selectively conduct both oxide ions and electrons through their lattice structure at elevated temperatures.[3] Under the influence of an oxygen partial pressure gradient, oxygen ions move through the dense, nonporous membrane lattice at high rates with 100 percent selectivity. Transported oxygen reacts with natural gas on the fuel side of the ceramic membrane in the presence of a catalyst to produce syngas.

In 1997 BP entered into an OTM Alliance with Praxair, Amoco, Statoil and Sasol to advance the Electropox technology in an industrially sponsored development program. These five companies

---

[1]Mazanec, T. J.; Cable, T. L.; Frye, J. G., Jr.; US 4,793,904, 27 Dec **1988**, assigned to The Standard Oil Company (now BP America), Mazanec, T. J.; Cable, T. L.; US 4,802,958, 7 Feb **1989**, assigned to the Standard Oil Co. (now BP America), Cable, T. L.; Mazanec, T. J.; Frye, J. G., Jr.; European Patent Application 0399833, 24 May **1990**, published 28 November **1990.**

[2]Bredesen, R.; Sogge, J.; "A Technical and Economic Assessment of Membrane Reactors for Hydrogen and Syngas Production" presented at Seminar on the Ecol. Applic. of Innovative Membrane Technology in the Chemical Industry", Cetraro, Calabria, Italy, 1-4 May **1996**.

[3] Mazanec, T.J., *Interface*, **1996**; Mazanec, T.J., *Solid State Ionics*, 70/71, **1994** 11-19; "Electropox: BP's Novel Oxidation Technology", T.J. Mazanec, pp 212-225, in "The Role of Oxygen in Improving Chemical Processes", M. Fetizon and W.J. Thomas, eds, Royal Society of Chemistry, London, **1993**; "Electropox: BP's Novel Oxidation Technology", T.J. Mazanec, pp 85-96, in "The Activation of Dioxygen and Homogeneous Catalytic Oxidation", D.H.R. Barton, A. E. Martell, D.T. Sawyer, eds, Plenum Press, New York, **1993**; "Electrocatalytic Cells for Chemical Reaction", T.J. Mazanec, T.L. Cable, J.G. Frye, Jr.; Prep Petrol Div ACS, San Fran, **1992** *37*, 135-146; T.J. Mazanec, T.L. Cable, J.G. Frye, Jr.; *Solid State Ionics*, **1992**, 53-56, 111-118.

have been joined by Phillips Petroleum and now are carrying out a multi-year $40+ million program to develop and commercialize the technology. The program targets materials, manufacturing and engineering development issues and culminates in the operation of semi-works and demonstration scale prototype units.

The Electropox process represents a truly revolutionary technology for conversion of natural gas to synthesis gas not only because it combines the three separate unit operations of oxygen separation, methane oxidation and methane steam reforming into a single step, but also because it employs a chemically active ceramic material in a fundamentally new way. On numerous fronts the commercialization of Electropox demands solutions to problems that have never before been accomplished. Basic problems in materials and catalysts, membrane fabrication, model development, and reactor engineering all need solutions to achieve commercial success. Six important issues have been selected as needing understanding on a fundamental level at which the applied Alliance program cannot achieve the breadth and depth of understanding needed for rapid advancement. These issues include:

1. Oxygen diffusion kinetics (University of Houston);
2. Phase stability and stress development (University of Missouri - Rolla);
3. Mechanical property evaluation in thermal and chemical stress fields (University of Alaska Fairbanks)

Statement of Work

Task 1 *Evaluate phase stability and thermal expansion of candidate perovskite membranes and develop techniques to support these materials on porous metal structures.*

Task 2 *Determine materials mechanical properties under conditions of high temperatures and reactive atmospheres.*

Task 3 *Measure kinetics of oxygen uptake and transport in ceramic membrane materials under commercially relevant conditions using isotope labeling techniques.*

EXECUTIVE SUMMARY

Research on the Oxygen Transport Membranes as identified in tasks 1-3 are being performed at the various universities under the stewardship of Praxair. The quarterly technical report presents the progress of the tasks defined to understand the fundamental concepts and structural performance of the OTM material.

In the current research, the oxygen occupancy was investigated at 1200^{o}C as a function of oxygen activity and compared with that at 1000^{o}C. The cause of bumps at about 200^{o}C was also investigated by using different heating and cooling rates during TGA. The TGA measurements were carried out as a function of temperature in air and as a function of oxygen activity at 1200^{o}C. The bumps were also observed at near 200^{o}C during heating and cooling in air in the current research. To investigate these bumps, weight changes of the bumps were measured at different heating and cooling rates and compared each other.

Fracture toughness of the LSFT and dual phase membranes were calculated using the Vicker's indentation method. The fracture toughness of the LSFT membrane was 1.6 MPa.m$^{1/2}$ and it is slightly higher than the dual phase membrane. An extensive analysis of the crack propagation behavior confirms the toughening mechanisms involved in determining the fracture toughness are the grain bridging, crack branching and the crack deflection. In the LSFT membrane the grain bridging was found to be the most prominent toughening mechanism. This may be due to the intergranular fracture behavior of the membrane. In the case of LSFT-CGO membrane, however, the prominent toughening mechanism was crack deflection due to the dense aggregation.

We have continued to investigate the thermodynamic properties (stability and phase-separation behaviour) and total conductivity of prototype membrane materials. The data are needed together with the kinetic information to develop a complete model for the membrane transport. We have previously reported characterization, stoichiometry, conductivity, and dilatometry measurements for samples of $La_{0.2}Sr_{0.8}Fe_{0.55}Ti_{0.45}O_{3-x}$. In this period, we have investigated by transmission electron microscopy the microstructure of ferrites that show very slow kinetics in the intermediate pressure range. The data suggest that the non-equilibrium behavior is associated with the formation of nano-particles of a reduced component which re-react at long times.

In the area of isotope transient studies at steady state, the current quarter has been dominated by continued analysis of the data from the isotope transients and the analysis of the profile in the quenched membrane.

Task 1: Preparation and Characterization of Dense Ceramic oxygen Permeable Membranes

X.-D Zhou[1], Q. Cai[2], J. Yang[1], W. B. Yelon[1], W. J. James[1] and H. U. Anderson[1]

1. **Materials Research Center, University of Missouri-Rolla, Rolla, MO 65401**
2. **Department of Physics, University of Missouri-Columbia, Columbia, MO 65211**

Thermogravimetric analysis of $La_{0.2}Sr_{0.8}Fe_{0.55}Ti_{0.45}O_{3-\delta}$ as a function of PO_2 at the elevated temperatures

Experimental

The TGA measurements were carried out as a function of temperature in air and as a function of oxygen activity at 1200°C. The bumps were also observed at near 200°C during heating and cooling in air in the current research. To investigate these bumps, weight changes of the bumps were measured at different heating and cooling rates and compared each other. The heating and cooling rates used in this experiment were 0.5, 1 and 3°C/min. The details about the TGA system and oxygen activity control were described in the previous report. Table I shows the details of oxygen activities used at 1200°C

Table I. The oxygen activity used in this experiment at 1200°C

	Ratio	oxygen activity at 1200°C
Air	100%	0.21
0.01% O_2/99.99% Ar	Premixed 100%	$1x10^{-4}$
CO/CO_2	10/90	$8.9x10^{-10}$
CO/CO_2	50/50	$1.1x10^{-11}$

Results and Discussion

The reproducibility of TGA was very important to estimate oxygen occupancy (3-δ) or deficiency (δ) as a function of oxygen activity and temperature. Therefore the reproducibility of

TGA was verified again in the current research by measuring weight changes of LSFT between room temperature and 1200°C. Figure 2 exhibits very reliable reproducibility in terms of weight change of LSFT as a function of temperature when it is compared with the previous results in Figure 1. The averaged weight change between room temperature and 1200°C is 37.5mg which is equivalent to 0.07 in oxygen deficiency (δ). Since the oxygen occupancy (3-δ) as a reference point at room temperature was determined as 2.99 in the previous research, the oxygen occupancy at 1200°C was estimated as 2.92. The oxygen occupancies and corresponding weight changes at 1200°C were also measured as a function of oxygen activity and are shown in Figure 3 and 4.

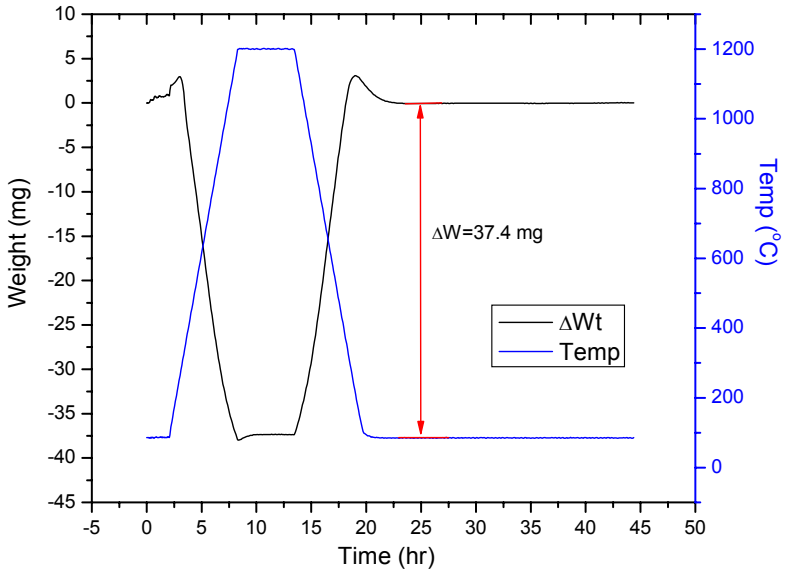

Figure 1 The weight change during annealing of $La_{0.2}Sr_{0.8}Fe_{0.55}Ti_{0.45}O_{3-\delta}$ measured by TGA between room temperature and 1200°C in air (from previous research)

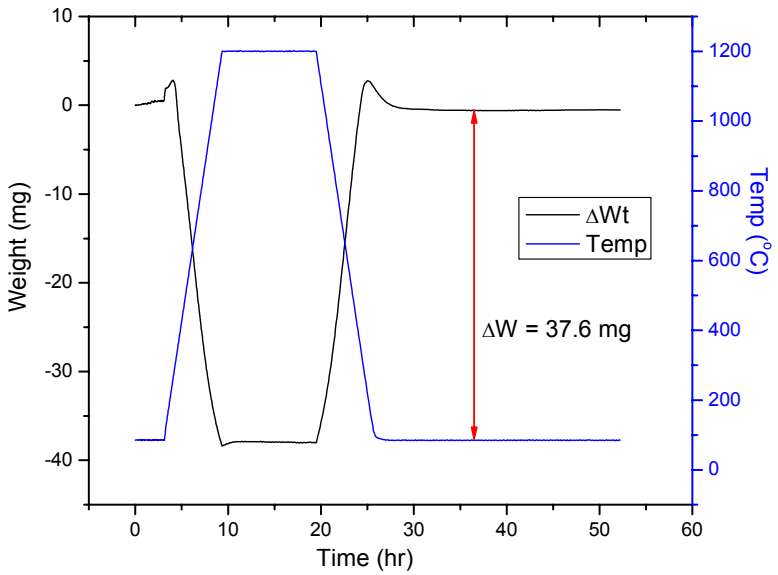

Figure 2 The weight change during annealing of $La_{0.2}Sr_{0.8}Fe_{0.55}Ti_{0.45}O_{3-\delta}$ measured by TGA between room temperature and 1200°C in air (from current research)

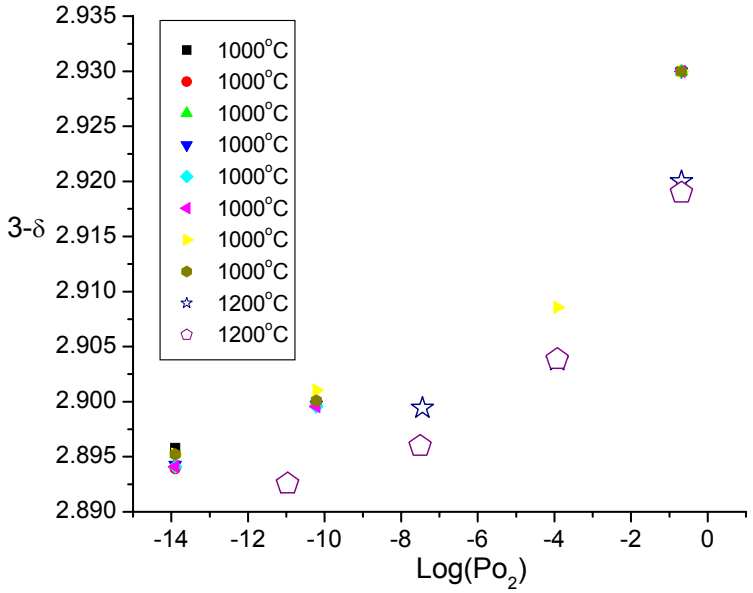

Figure 3 The oxygen occupancy of $La_{0.2}Sr_{0.8}Fe_{0.55}Ti_{0.45}O_{3-\delta}$ calculated using TGA at 1000 and 1200°C as a function of oxygen activity

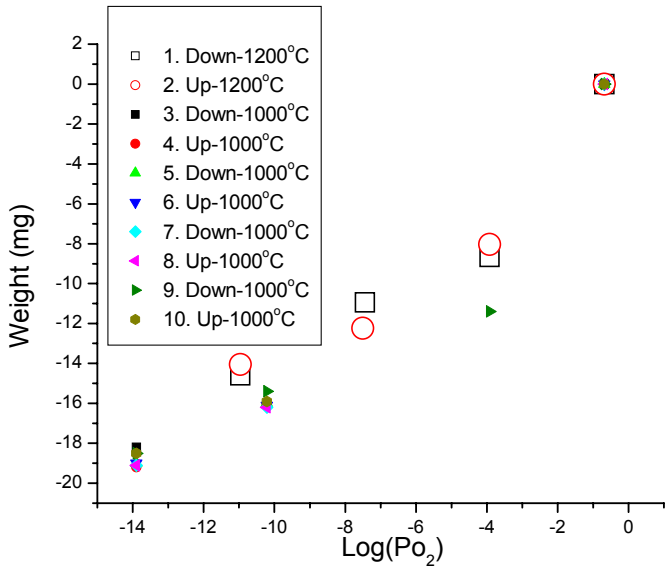

Figure 4. The weight loss of $La_{0.2}Sr_{0.8}Fe_{0.55}Ti_{0.45}O_{3-\delta}$ measured by TGA at 1000 and 1200°C as a function of oxygen activity

Figure 3 shows the comparison of oxygen occupancy changes at 1000 and 1200°C as a function of oxygen activity. The oxygen occupancy difference ($\Delta\delta$) is 0.004 and 0.005 at $1x10^{-11}$ and $1x10^{-4}$ of oxygen activity between 1000 and 1200°C which is equivalent to 2 and 3 mg. (Figure 4) The details of oxygen occupancies as a function of oxygen activity at 1000 and 1200°C are shown in Table II.

Table II. The oxygen occupancies (3-δ) as a function of oxygen activity at 1200°C

	Oxygen occupancy (3-δ) from current research at 1200°C (oxygen activity at 1200°C)	Oxygen occupancy (3-δ) from previous research measured at 1000°C (oxygen activity at 1000°C)
Air	2.92 (0.21)	2.93 (0.21)
0.01% O_2/99.99% Ar	2.90 ($1x10^{-4}$)	2.91 ($1x10^{-4}$)
CO/CO_2 = 10/90	2.90 ($8.9x10^{-10}$)	2.90 ($6.3x10^{-13}$)
CO/CO_2 = 50/50	2.89 ($1.1x10^{-11}$)	2.90 ($7.8x10^{-15}$)

The bumps at near 200°C during heating and cooling of LSFT were observed in the current research in Figure 5. In the previous report, high heating and cooling rate such as 3°C/min was suggested as a cause of bumps. To verify this suggestion, we used different heating and cooling rate during TGA and compared plots at about 200°C. (Figure 6) Figure 6 shows shape of plots, amount of weight change of each different heating and cooling rates and temperatures of maximum point. From the results, it was found that the fast heating and cooling rate was probably the main reason to explain the bumps. The heights of bumps were different when different heating and cooling rates were applied. The weight change was estimated at the maximum point of each bump when weight was set zero at room temperature. The weight differences between the maximum points were also calculated. The calculated weight difference was 0.7 mg between 3°C/min and 0.5°C/min. Therefore 0.7mg was considered to be an artifact when 3°C/min was used. However the bump still existed even at 0.5°C/min heating and cooling rate and was supposed to be due to the adsorption and desorption of oxygen or a phase change in

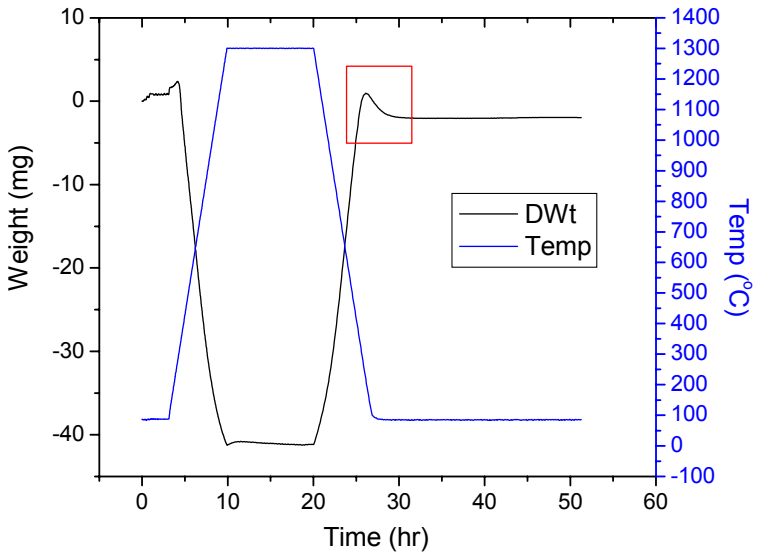

that temperature range. To verify this assumption, the quenching experiment and XRD study will be performed in the future.

Figure 5. The weight change during annealing of $La_{0.2}Sr_{0.8}Fe_{0.55}Ti_{0.45}O_{3-\delta}$ measured by TGA at 1300°C in air (heating/cooling rate is 3°C/min)

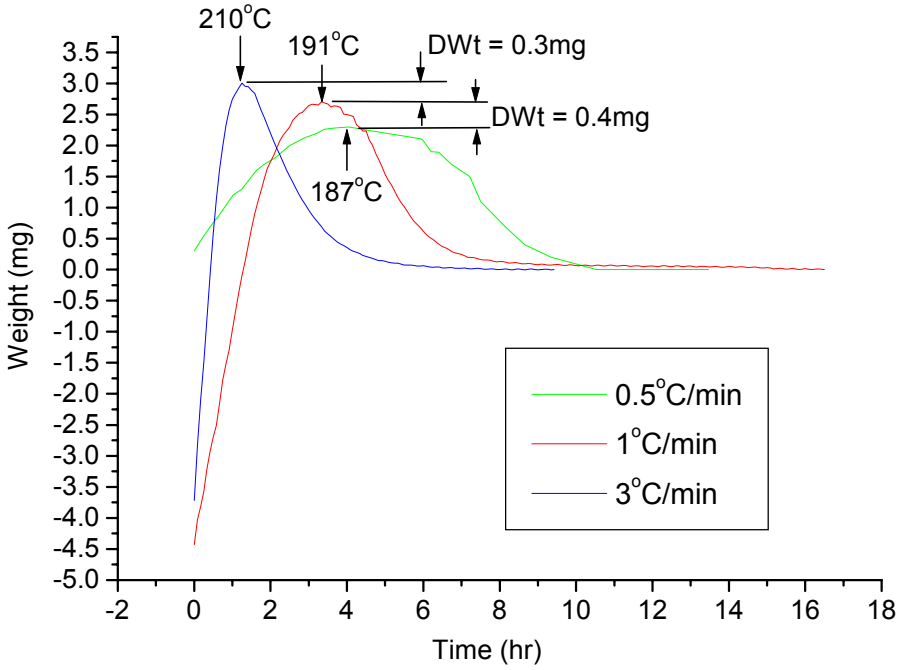

Figure 6. The weight change during cooling of $La_{0.2}Sr_{0.8}Fe_{0.55}Ti_{0.45}O_{3-\delta}$ near 200°C measured by TGA in air at cooling rate is 0.5, 1 and 3°C/min

Future studies

1. Electrical conductivity and Seebeck coefficient are being measured currently and will be discussed with TGA results in the next report.
2. TGA study at different temperature will be carried out.

TASK 2: Determine material mechanical properties under conditions of high temperature and reactive atmosphere

Prof. S. Bandopadhyay and Dr. T. Nithyanantham

Fracture toughness is defined as the resistance of a material to an advancing crack. Fracture toughness generally depends on the temperature, environment, loading rate, the composition of the material and its microstructure. The fracture toughness of the LSFT and LSFT-CGO membranes are generally studied using Vicker's indentation method. The fracture toughness determination with Vicker's hardness indentations was proposed by Evans and Charles (1976) and later extended and modified by Niihara *et al* (1982), Antis *et al* (1981) and Lawn *et al* (1980). Through this technique, a K_{Ic} (Mode-I Fracture Toughness) value is obtained by means of semi-empirical correlations between the indentation load and the length of the cracks emanating from the corresponding Vickers indentation impression. In the present investigation, in order to understand the strengthening mechanisms involved in the non-transforming La based ceramic composites, cracks were generated using Vicker's indenter and used to identify and evaluate the toughening mechanisms.

Experimental:

The LSFT and dual phase membranes were cut and ground down to 600 grade SiC paper prior to the analysis. The indentations were made using loads starting from 0.98 to 9.8N to initiate the cracks. The indentation was given for 10 sec in all loads. The cracks were generated only at the load of 9.8N which was the maximum achievable load in the machine that was used. No observable cracks were produced at lower loads. The indentations were immediately analyzed using SEM since measuring the crack lengths using optical microscope was difficult.

In Fig 7 the development of Vicker's indentation cracks are illustrated. As it can be seen that below the Vickers pyramid a deformation zone develops.

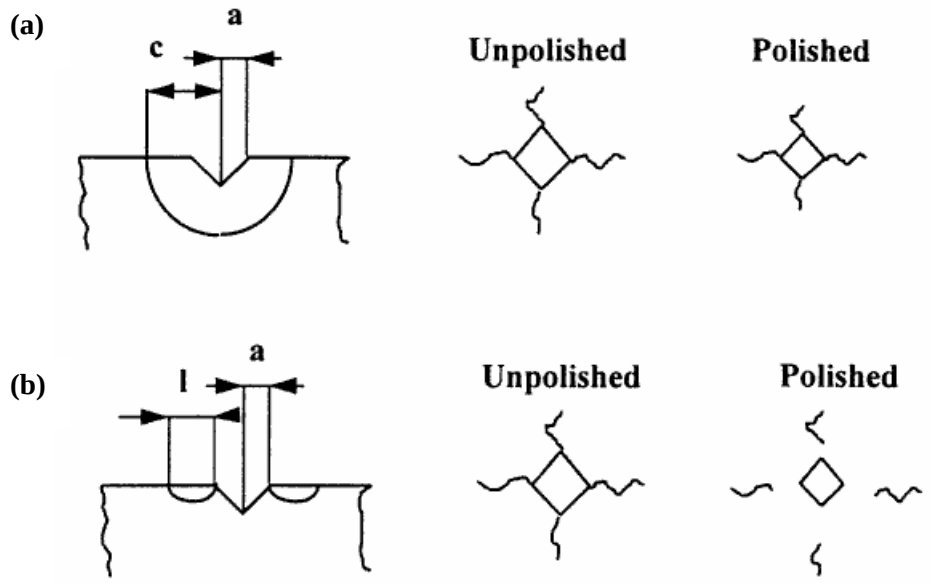

Figure 7. (a) Median and (b) Palmqvist crack systems induced by Vickers indentation.

During loading and unloading two perpendicular cracks are initiated starting at the deepest location of the deformation zone and propagate to the specimen surface. The final crack is nearly in a half penny shape (Median cracks). The crack length at the surface is 'c'(from the center of the indentation diagonal) and the length of the indentation diagonal is 2a. For some materials (with relatively high toughness) a different crack system develops. In these situations, radial shallow cracks occur directly below the surface. These cracks are called Palmqvist cracks. The length of the Palmqvist cracks 'l' is measured from the ends of the impression diagonals (Figure 7-b). Therefore, the crack length, c, can be written as (a+l).

The hardness of the membranes was calculated from the diagonal length (equation 2.1) and the Young's modulus of the materials was assumed to be 123GPa, where as, Ø is the constraint factor which is approximately 3.0 for ceramics. Figure 8 shows the impression of the indentation with cracks emanating from the corners.

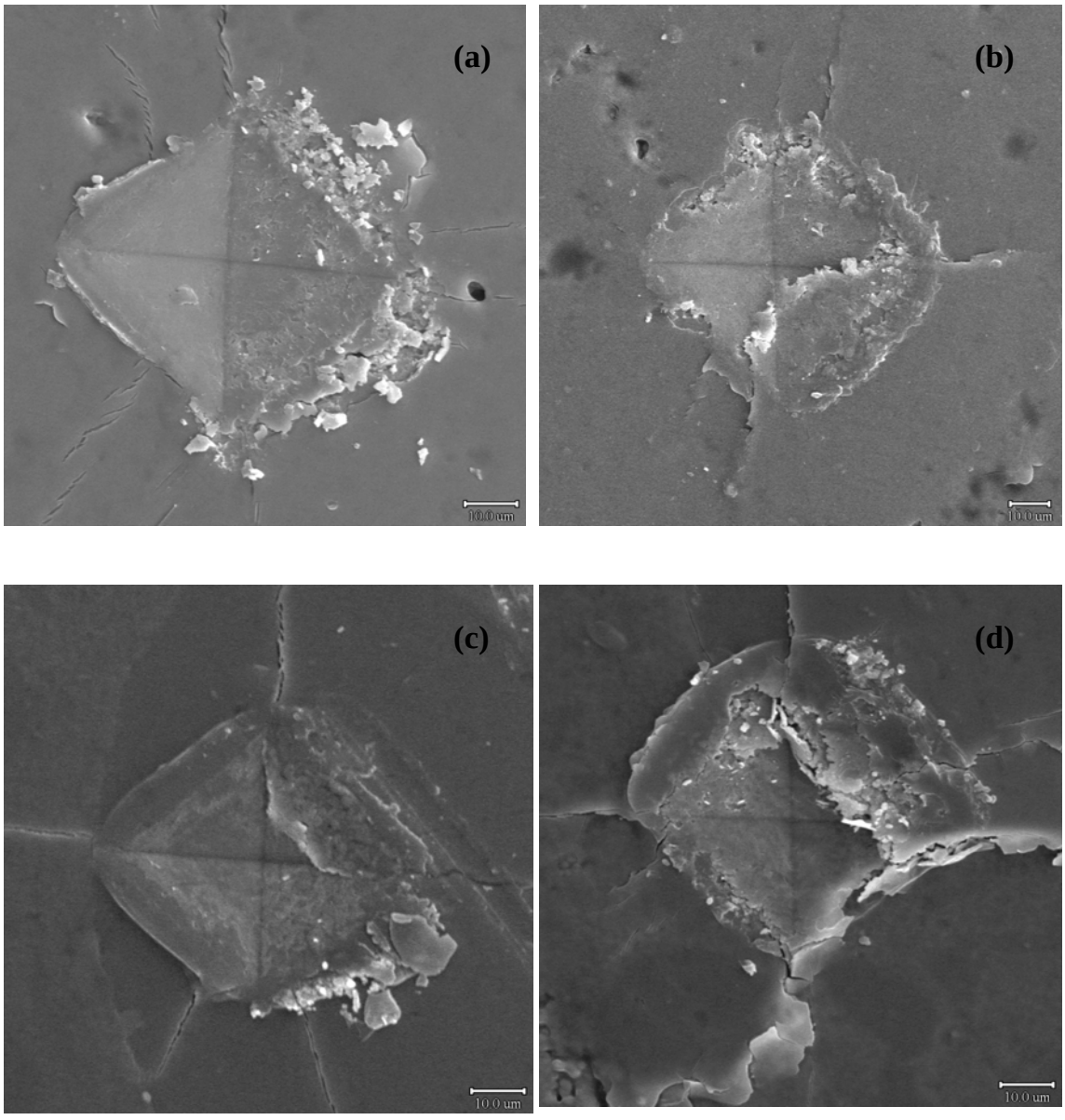

Figure 8. Vicker's indentations in (a-b) LSFT membrane and (c-d) in dual phase membrane. Note in the LSFT-CGO the crack patterns are mainly median cracks and in dual phase the Palmqvist cracks are also seen (in Fig8-a). In Figure 8-c the indentation is in the dense region where as in Figure 8-d the indentation is on porous region.

Crack lengths were measured and the l/a and c/a values were calculated to verify the conditions. Appropriate formulas were used to calculate the fracture toughness and the results were compared. Niihara et al. (1982) equations for the Palmqvist cracks ($0.25 \leq l/a \leq 2.5$) is given in equ. 2.1.

$$\left(\frac{K_{IC}\,Ø}{H\sqrt{a}}\right)\left(\frac{H}{EØ}\right)^{0.4} = 0.035(l/a)^{-0.5} \qquad \text{--- (2.1)}$$

and that for the median cracks ($c/a \geq 2.5$) is

$$\left(\frac{K_{IC}\,Ø}{H\sqrt{a}}\right)\left(\frac{H}{EØ}\right)^{0.4} = 0.129\,(c/a)^{-1.5} \qquad \text{--- (2.2)}$$

where,

K_{IC} is the Mode I critical stress intensity factor (MPa.m ^{½})
Ø is the constraint factor (≈ 3.0)
H is the Vickers hardness (GPa)
E is the Young's modulus (GPa)
a is the half diagonal of the Vicker's indent (m)
c is the radius of the surface crack (median) (m) and
l is the crack length (Palmqvist) (m)

For comparison the K_{IC} values were calculated by using the following formula suggested by Evans and Charles (1976) which do not use the elastic modulus of the membranes.

$$K_{IC} = 0.16\,H_v\,a^{½}\,(c/a)^{-3/2} \qquad \text{--- (2.3)}$$

The fracture toughness values of the LSFT and dual phase membranes are tabulated in Table 1 and Table 2 respectively.

In the LSFT membrane, the cracks emanated from the indentation impression were mainly Palmqvist type. Hence, the fracture toughness values calculated using the equation 2.1 are relatively higher than that of the values calculated using the two other methods. The difference between the values calculated by the equations 2.1 and 2.2 is not significant.

Table 1. Fracture toughness of the LSFT membrane

Crack Length					a (m) E-5	H_v (GPa)	K_{IC} [1] ($MPa.m^{1/2}$)	K_{IC} [2] ($MPa.m^{1/2}$)	K_{IC} [3] ($MPa.m^{1/2}$)
L1 (μm)	**L2 (μm)**	**L3 (μm)**	**L4 (μm)**	**L (m)** E-5					
39.3	42.76	73.45	31.94	4.68625	2.881	5.47	1.45	1.59	1.1
63.18	--	32.02	45.46	4.68867	2.54525	7.01	1.48	1.55	1.19
33.78	31.96	50.66	38.02	3.8605	3.05925	4.85	1.58	1.92	1.26
35.96	40.88	40.23	32.1	3.72925	3.0595	4.85	1.6	1.97	1.3
41.01	56.25	34.16	--	4.38067	2.817	5.72	1.5	1.69	1.19
41.36	67.43	--	39.71	4.95	2.8545	5.57	1.41	1.52	1.05
48.37	63.42	36.46	--	4.94167	2.86475	5.53	1.41	1.52	1.05
66.78	65.39	47.62	34.69	5.362	3.1115	4.69	1.33	1.44	0.93
44.25	56.88	44.6	26.58	4.307	2.78525	5.85	1.52	1.72	1.22
37.13	57.82	37.67	44.41	4.425	3.048	4.89	1.47	1.7	1.12
69.7	59.34	53.76	--	6.09333	2.90175	5.39	1.26	1.24	0.85
59.14	69.12	45.28	43.22	5.419	3.0835	4.77	1.33	1.42	0.93
--	--	50.48	--	5.048	3.1827	4.48	1.37	1.53	0.97
54.69	48.44	47.26	36.25	4.666	2.939	5.26	1.46	1.61	1.1
36.77	28.3	50.01	46.56	4.041	2.8202	5.71	1.56	1.82	1.28
43.71	55.68	--	--	4.969	3.0935	4.74	1.39	1.54	1.0
41.01	46.21	29.35	49.15	4.143	2.8707	5.51	1.54	1.79	1.24
52.07	56.17	47.11	42.11	4.936	2.78	5.87	1.42	1.51	1.07

1. Equation 2.1
2. Equation 2.2
3. Equation 2.3

Table 2. Fracture toughness of the LSFT-CGO membrane

Crack Length					a (m) E-5	H_v (GPa)	K_{IC} [1] ($MPa.m^{1/2}$)	K_{IC} [2] ($MPa.m^{1/2}$)	K_{IC} [3] ($MPa.m^{1/2}$)
L1 (µm)	**L2 (µm)**	**L3 (µm)**	**L4 (µm)**	**L (m)** E-5					
38.35	79.44	87.42	--	6.84033	2.68175	6.32	1.22	1.07	0.78
--	--	--	--	--	2.77575	5.9	--	--	--
--	--	--	--	--	2.61025	6.67	--	--	--
46.43	42.29	48.68	54.37	4.79425	2.6055	6.69	1.46	1.53	1.14
48.52	61.87	53.18	55.45	5.4755	2.744	6.04	1.35	1.36	0.98
--	--	--	--		2.78475	5.86	--	--	--
43.16	43.75	43.42	62.71	4.826	2.3585	8.17	1.48	1.47	1.19
64.47	58.06	45.21	71.92	5.9915	2.381	8.01	1.33	1.18	0.95
72.96	93.85	40.73	57.07	6.61525	2.186	9.50	1.29	1.02	0.88
89.68-	58.16	54.5	45.58	5.27467	2.372	8.07	1.42	1.35	1.09
58.77	101.03	50.92	42.44	6.329	2.4542	7.54	1.29	1.13	0.88
61.96	53.54	72.37	91.88	6.99375	2.436	7.65	1.23	1.01	0.79
64.88	72.16	65.09	--	6.73767	2.8342	5.65	1.21	1.11	0.78
69.34	61.54	48.02	50.18	5.727	2.5195	7.16	1.35	1.26	0.97
60.84	--	--	--	6.084	2.57	6.88	1.30	1.19	0.9
90.07	75.56	53.79	50.35	6.74425	2.34	8.3	1.26	1.03	0.84
67.77	63.27	--	70.79	6.72767	2.45675	7.53	1.25	1.05	0.83

1. Equation 2.1
2. Equation 2.2
3. Equation 2.3

In the dual phase membrane, the cracks are predominantly median (c/a ≥ 2.5) type. The fracture toughness values are given in Table 2. In the dual phase membrane, the crack length is controlled by the microstructure. In Figure 8-c, the indentation is made on a dense region where as in Figure 8-b the indentation has fallen on a porous region. The heterogeneity of the microstructure causes a scatter in the hardness values (Table 2). Initiation and propagation of cracks are also significantly affected by this microstructural inhomogeneity (Figure 9).

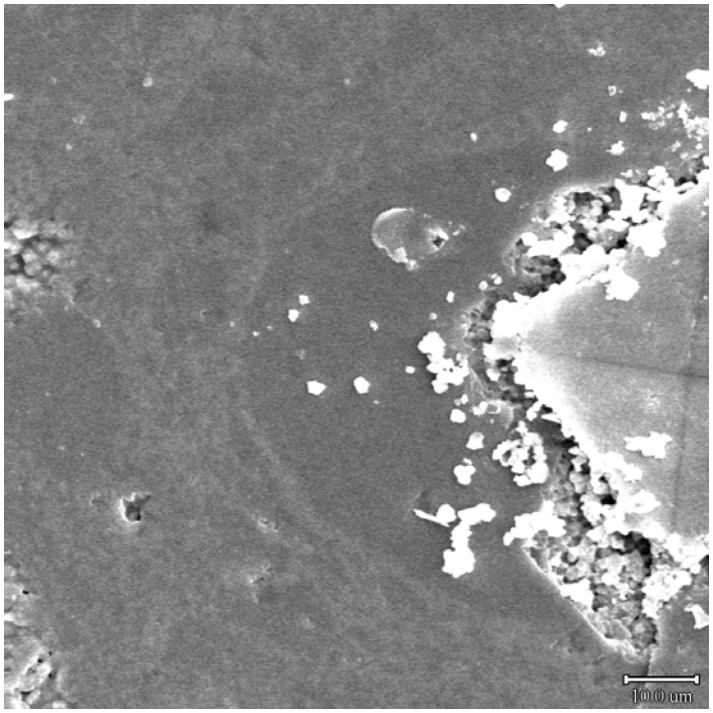

Figure 9. Influence of microstructural heterogeneities on initiation and propagation of cracks. The indentation is made on the dense region in the dual phase microstructure. While the crack has not formed in the dense region, a crack has emanated from the diagonal that is closer to the porous region.

The fracture toughness of the LSFT-CGO is slightly inferior to the LSFT. The reason for the inferior fracture toughness of the dual phase can be analyzed by studying the crack propagation behavior. In general, the fracture toughness of the LSFT membranes was low and slightly higher than the window glass. In the case of LSFT membrane, the cracks are mainly Palmqvist type. But the cracks that are generated in the dual phase membrane were Median type. The fracture toughness values of dual phase membrane that were calculated from the crack length also support the Median crack types. The c/a ratio of the cracks was ≥ 2.5 in the LSFT-CGO membrane and the K_{IC} values were inferior to the K_{IC} values of LSFT membrane. The K_{IC} values of both the membranes that were calculated without using the Young's modulus were significantly inferior to the rest of the values.

Crack Propagation behavior:

Enhancing the toughness of non-transforming ceramics depends primarily on the events which occur beyond rather than at or ahead of the advancing crack. It has been acknowledged that several toughening events may take place together and that the combined effect is not necessarily a simple liner combination of the individual effects. In the present investigation, in order to understand the strengthening mechanisms involved in the non-transforming La based ceramic composites, cracks were generated using Vicker's indenter. Even though the crack evolutions that are shown in the figures are representations of LSFT and dual phase membranes, they need not be considered as the characteristics crack patterns of the respective membrane or loading conditions since the crack can not be exactly reproduced.

Crack propagation in the LSFT membrane:

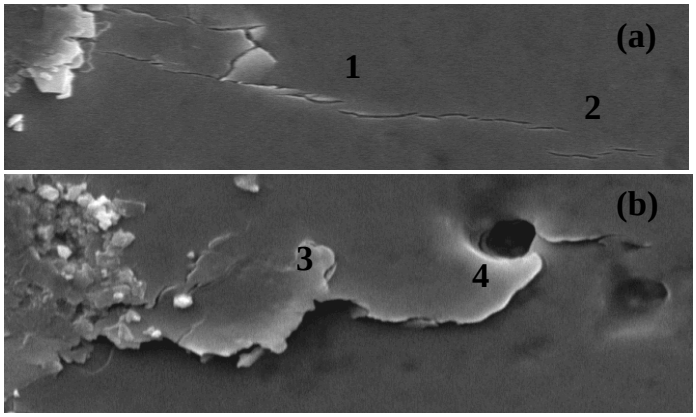

Figure 10. Crack propagation in the LSFT membrane
(a) grain bridging
(b) crack deflection by boundaries and pores

The predominant toughening mechanisms are grain bridging, crack branching and crack deflection. In Figure 10 shows apparently isolated segments at site 1 and 2 which get connected together in a common crack interface. In site 3, it can be noted that the lower crack segment enclosing the bridging grain has over-linked up with a crack branch to lead a rupture of the bridging grain. Another crack front that advanced further was deflected by a pore and eventually got arrested (at site 4).

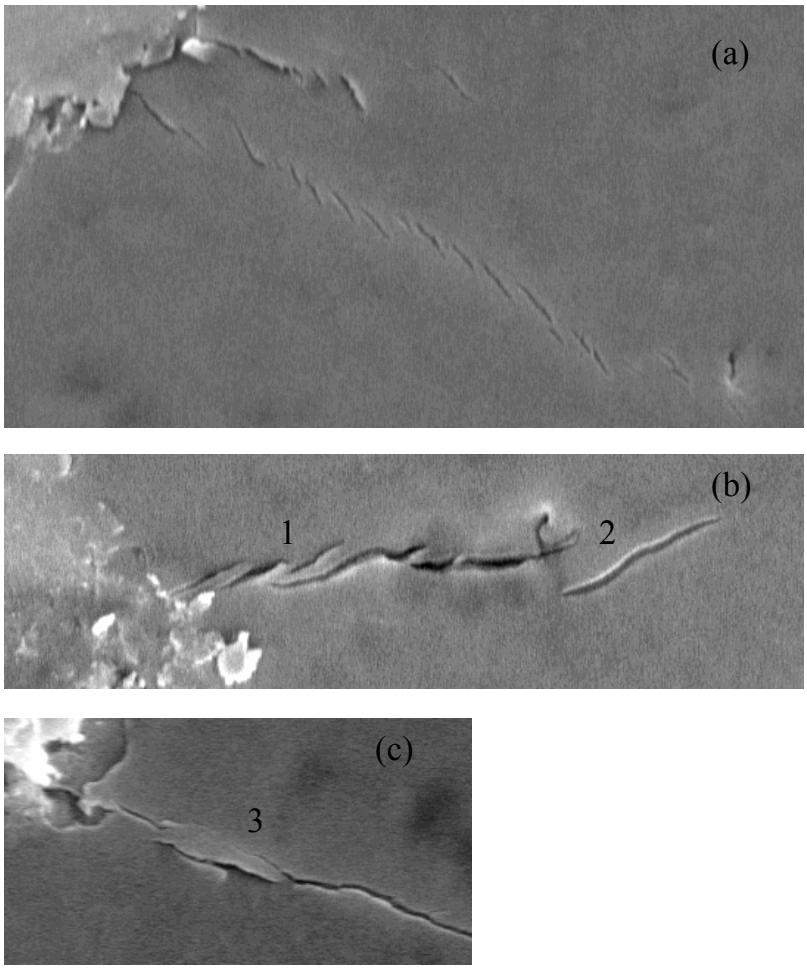

Figure 11. Discontinuous crack and rupture of bridging grain. Note the extensive grain bridging all along the crack length (Fig 5.a). A closer observation of the other crack reveals the effect of bridging ligaments on closing the crack propagation (Fig 5.b). Final rupture of the grain (Fig 5.c)

Figure 11 (a and b) shows the several discontinuous (segmented) crack traces on the membrane surface. However the crack segments connect beneath the surface into a common, primary crack interface. In the discontinuous crack, the bridging ligaments (at site 1) exert closing forces which reduce the stress intensity at the crack tip and additional stress is needed to break the interfacial bonding. Site 2 (in Fig 11.b) shows a particularly large bridging behind the tip of an extended crack. It is evident that this bridging has spent most of the crack energy and stopped the crack growth. The final rupture of the bridging grain can be seen at site 3.

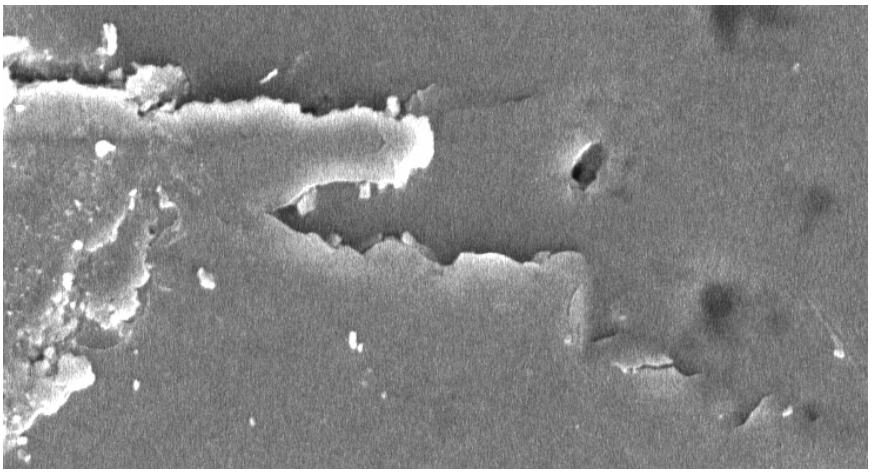

Figure 12. Surface traction in an advancing crack caused by frictional interlocking of grains

Figure 12 shows the frictional interlocking of grains on the fracture causes surface tractions. Each source of traction acts to shield the crack tip from the applied stress, by spending the stress in friction. The frictional interlocking tries to 'trap' the growing crack. Hence, more energy is needed to advance the crack front.

Crack propagation in the dual phase membrane:

All the common toughening mechanisms that were involved in the single phase membrane are also active in the dual phase. Furthermore, in the dual phase membrane, the inherent microstructural feature is due to the distribution of dense regions in the continuous porous region. The crack deflection is an important toughening mechanism which contributes to approximately ≈ 40% of the fracture resistance in the composite. The crack is likely to be deflected at the interface when it approaches a dense region or cluster.

Figure 13. Crack bridging by dense region in the dual phase membrane.

Figure 13 shows the crack bridging caused by a dense region. The crack appears very weak after the bridging event since it has traveled a long distance along the dense region's interface.

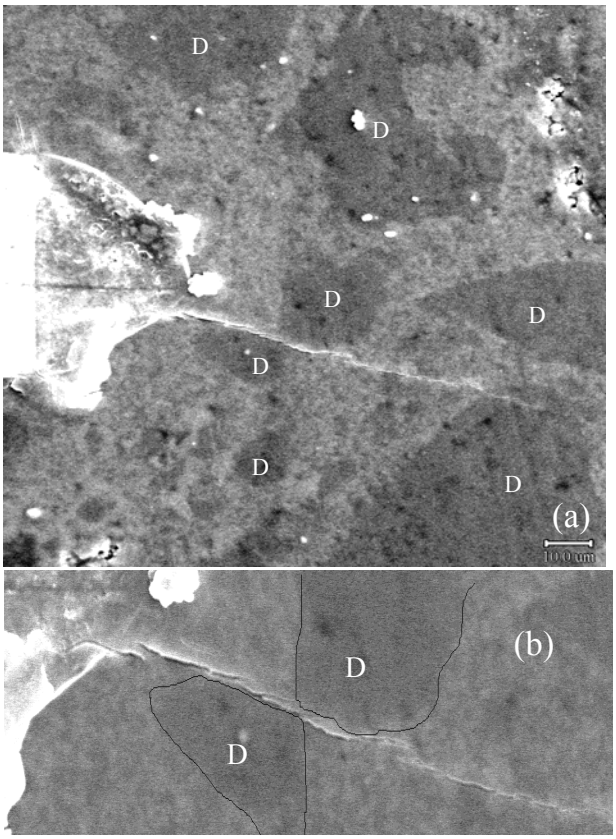

Figure 14. Crack propagation behavior in the dual phase membrane. Crack deflection by the dense regions.

Figure 14 shows a typical crack propagation behavior in the dual phase membrane. The crack emanated from the indentation was deflected by a dense aggregate and taken the path along the boundary of the aggregate and exactly passes between two dense regions. Normally the interfacial region around a dense region or an aggregate will be weak due to the thermal expansion mismatches or differential shrinkage of the constituent phases. Hence the crack propagation will be always preferred along the interface. In the LSFT-CGO membrane the crack has continued its propagation in the less dense region rather than choosing the boundaries of the dense region. It proves that the discontinuous dense regions and the surrounding porous region have a strong interface.

Figure 15 shows the crack branching and interlocking of grains. The crack experiences the crack bridging (site 1) and eventually halts. The growth of the other branch of the crack has been arrested by a strong frictional interlocking mechanism (site 2) that took place behind the crack tip.

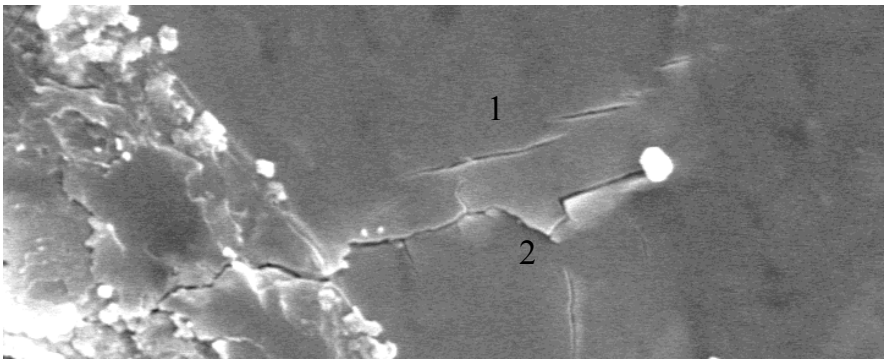

Figure 15. Crack branching and frictional interlocking of grains

Plans for the next quarter:

1. Thermomechanical studies will be carried out on dual phase membranes.
2. Necessary x-ray diffraction analysis will be done on the fractured samples
3. Thermal analysis will be carried out at various environments.

Task 3: **Measurement of Surface Activation/Reaction Rates in Ion Transport Membranes using Isotope Tracer and Transient Kinetic Techniques**

A. J. Jacobson, University of Houston, C.A. Mims, University of Toronto

EXPERIMENTAL

Most of the work at UH this quarter has been directed towards experiments on the non-equilibrium behavior of $La_{0.2}Sr_{0.8}Fe_{0.55}Ti_{0.45}O_{3-\delta}$. Samples of this composition prepared and characterized as previously reported were quenched in pellet form from a series of oxygen partial pressures at 900 ºC. The pO_2 values were 1.25×10^{-4} atm, 1.11×10^{-7} atm, 1.70×10^{-10} atm, and 6.74×10^{-14} atm. After the quench X-ray patterns were recorded. The X-ray patterns show little or no evidence other than a pure perovskite phase. The lattice parameter increases systematically as the pO_2 decreases as can be seen for the two reflections shown in Figure 16.

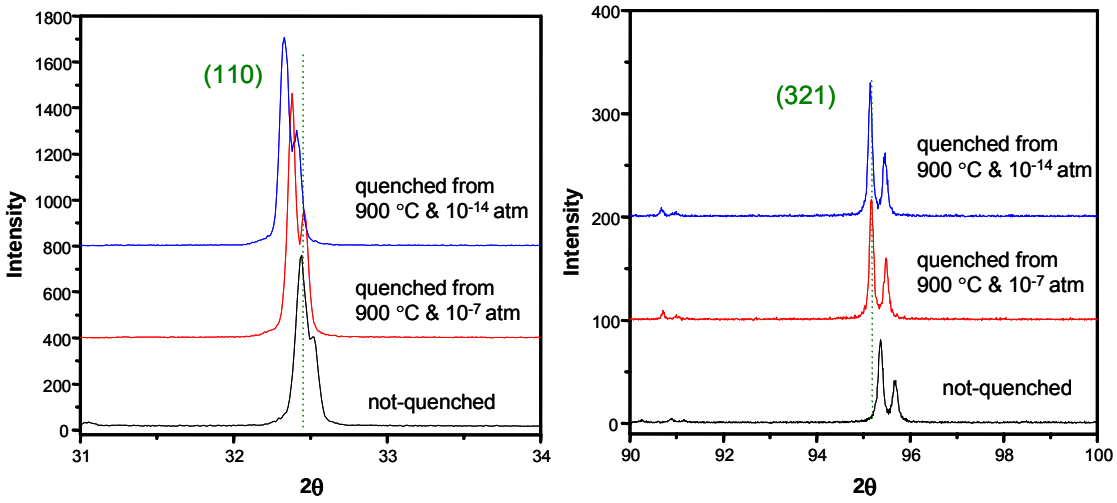

Figure 16. Representative X-ray patterns for quenched samples of LSFTO.

Specimens for electron microcopy study were prepared from the quenched samples by cutting slices, polishing and the thinning using a Gatan ion mill. The samples were examined in a JEOL 2020F high resolution transmission electron microscope.

The other experimental techniques used to generate the results reported here have been described in previous quarterly reports

RESULTS AND DISCUSSION

University of Houston

Non-equilibrium behavior

We have continued to investigate the thermodynamic properties (stability and phase-separation behavior) and total conductivity of prototype membrane materials. The data are needed together with the kinetic information to develop a complete model for the membrane transport. We have previously reported characterization, stoichiometry, conductivity, and dilatometry measurements for samples of $La_{0.2}Sr_{0.8}Fe_{0.55}Ti_{0.45}O_{3-x}$. In this report, we have started to investigate the non equilibrium behavior observed in conductivity and thermal expansion previously reported.

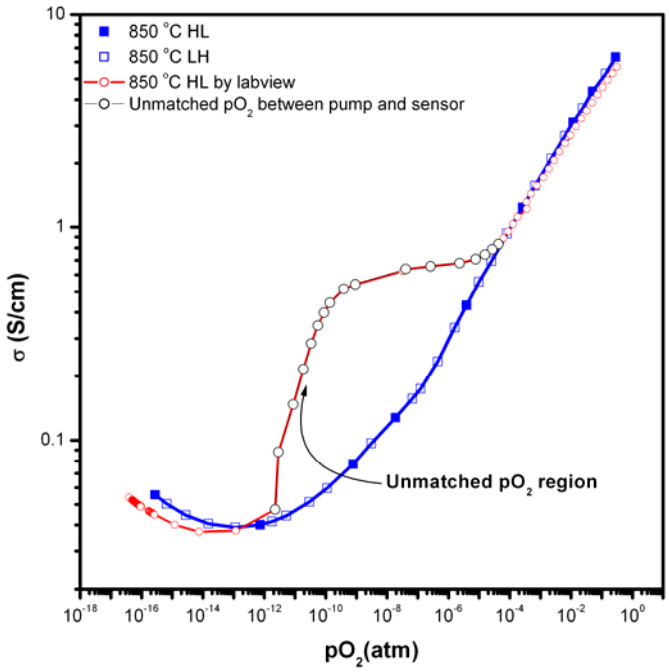

Figure 17. Conductivity measurements for LSFTO showing the non-equilibrium behavior in the intermediate pressure range.

Similar, extremely slow equilibrium kinetics were also observed in the Seebeck coefficient measurements previously reported. The effects in the conductivity data at 850 ºC are illustrated in Figures 17.

An understanding of this behavior is needed to predict membrane performance on pO_2 cycling. To address the question, we have examined quenched samples by high resolution transmission electron microscopy. Samples of LSTO in the form of dense ceramic disks were quenched from different pO_2 values that span the range of behavior from 900 ºC. Preliminary results indicate significant differences in microstructure for the samples quenched from the different partial pressures. Results for the sample quenched from 1.25×10^{-4} atm are shown in Figures 18 and 19. The sample was observed to have two distinct microstructures. In one region, the sample has the perovskite structure with very few defects. This is shown in Figure 18 for a [100] projection. [110] and [111] were also found to be similar.

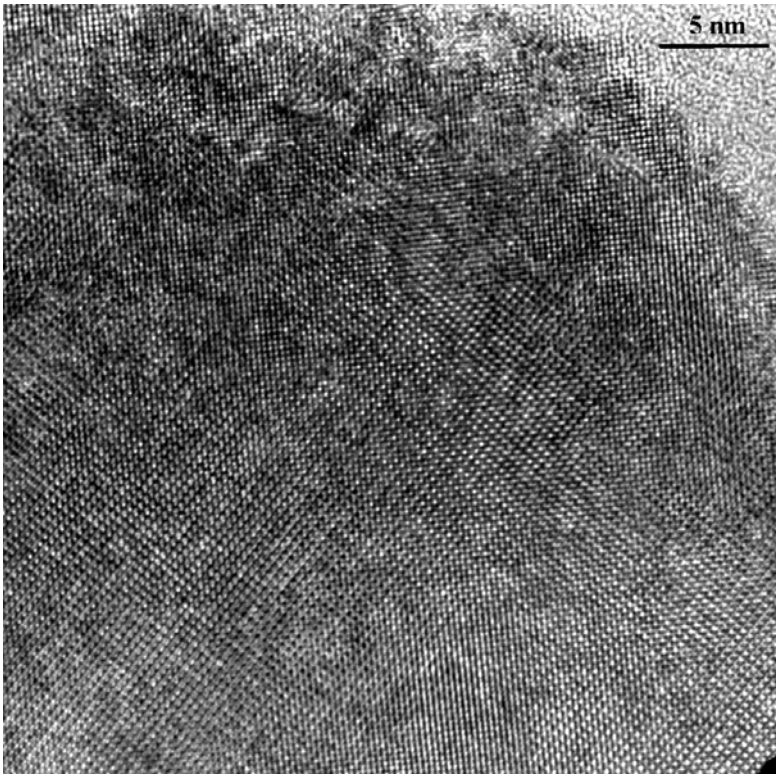

Figure 18. The [100] projection of region 1 found in the structure of LSFTO quenched from 900 C and $pO_2 = 1.25 \times 10^{-4}$ atm.

In contrast the microstructure observed in other regions of the sample was quite different. A low magnification image of region 2 is shown in Figure 18. In addition to the grain boundary, the microstructure contains many small (~ 5-10 nm domains) that are roughly circular. At higher resolution these regions are clearer and can be seen to be crystalline. Detailed analysis of the structure of the central particle by Fourier inversion gives a lattice constant that corresponds to iron metal and not to that of any iron oxide phases. The current model based on these results is

that the perovskite phase has an easy kinetic pathway to reduction that eliminates oxygen vacancies by forming metallic iron. We propose a general mechanism as indicated below

$ABO_3 \rightarrow ABO_{3-x} \rightarrow A_2BO_4 + AO \rightarrow A_2BO_4 + B$ or alternatively $ABO_3 \rightarrow ABO_{3-x} \rightarrow$ 'ABO_x' $+AO \rightarrow$'ABO_x' $+B$ where 'ABO_x' is an amorphous phase.

We see no evidence in the microstructure as yet for the presence of the 214 phase so the second mechanism may be more likely. We note however, the recent observation that in thin film synthesis of $La_{0.5}Sr_{0.5}FeO_{3-x}$, the phases formed under reducing conditions are 214 $LaSrFeO_4$ and Fe. We plan to next examine this composition in bulk form to compare the results with the thin film data.

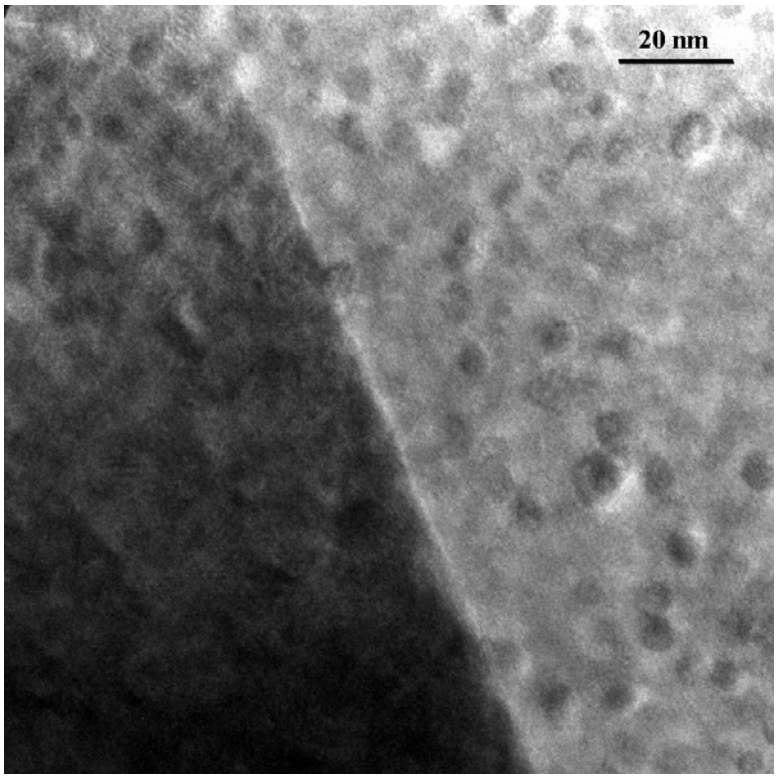

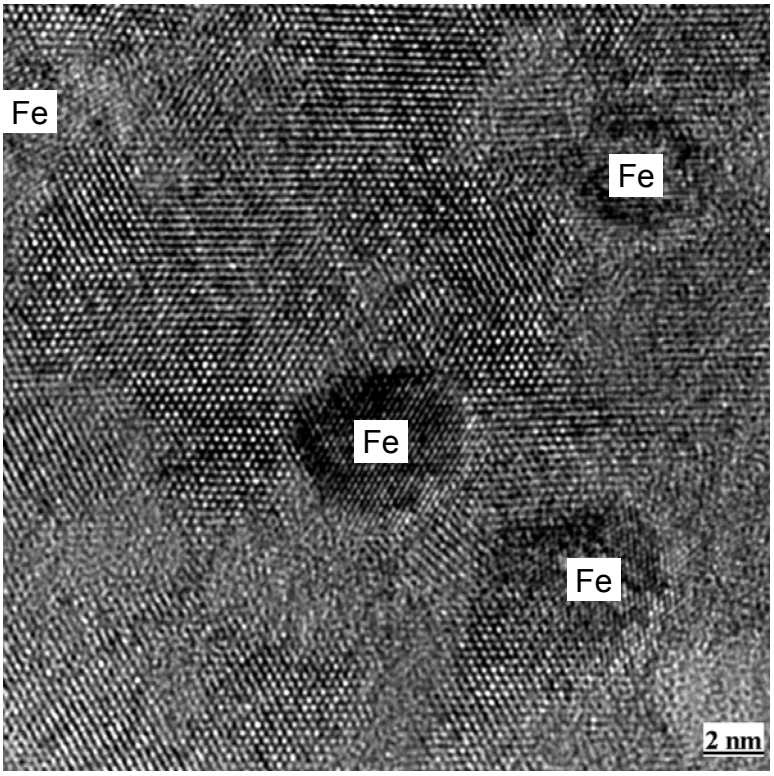

Figure 19. Electron micrographs of region 2 in the structure of LSFTO quenched from 900 C and $pO_2 = 1.25 \times 10^{-4}$ atm.

Plans for next quarter

In the next quarter we will complete analysis of the TEM results and examine quenched samples of $La_{0.5}Sr_{0.5}FeO_{3-x}$.

University of Toronto

Isotope Transient Studies at Steady State

As set forth in previous reports, the various surface and bulk transport parameters can be separately determined on an operating membrane by the application of an isotopic transient (a pulse of $^{18}O_2$ in our case) on one side of an operating membrane and the subsequent time dependence of ^{18}O evolution from both sides of the membrane. Both the forward and reverse surface rates can be directly measured. In flux measurements, only the net rates are available. Many such experiments can be performed on one sample, thus removing the sample-to-sample variability in IEDP experiments. In addition, sacrifice of the membrane during a transient allows

internal gradients at steady state to be revealed. This aspect is the focus of the last quarter's work at Toronto.

Summary of progress:

Determination of internal diffusivity gradients in quenched isotope profiles:

In the previous report, the ^{18}O SIMS profile from an LSCrF membrane under high oxygen gradient conditions, with a CO/CO_2 mixture on the outside and 20% oxygen on the inside of the membrane, and which was quenched during an isotope transient experiment was presented. One of the profiles measured in a radial cross section is shown below.

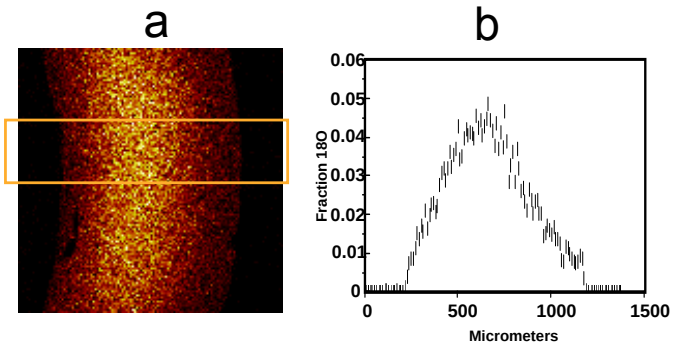

Figure 20. ^{18}O radial intensity map (a) and isotope profile (b) from a tubular membrane of $La_{0.2}Sr_{0.8}Fe_{0.8}Cr_{0.2}O_{3-x}$ quenched during an isotope transient at steady state.

The conditions were 900 ºC with 0.2 atm O_2 on inside (left) and 0.5 atm of $CO_2/CO = 1$ on the outside (right). A distinctive asymmetry is evident in the quenched profile with a shallower slope to the outside surface than to the inside surface.

During the past three months, these results have been analyzed using a 1-D model to simulate the evolution of the isotope distribution during the transient. Previous modeling efforts under low oxygen gradients on LSCF (air separation conditions) were able to successfully fit the isotope distribution (both the time-dependent behavior in the delivered oxygen and the profile "frozen" in the internal profile) with a constant value of the oxygen diffusivity throughout the membrane. Under conditions where a high chemical gradient exists across the membrane, the diffusivity is expected to vary significantly through the bulk. Such a variation is reflected in the internal isotope distribution, though not readily evident in the isotope transient in the delivery-side gas phase.

Figure 21 shows two calculated internal isotope distributions during an isotope transient. The parameters were chosen to replicate the behavior of the membrane under the experimental conditions which produced the profile in Figure 20. Two simulations are shown, one with constant Do of 5×10^{-7} cm^2/s (open circles) and the other with a linear gradient (solid line), increasing from 2.2×10^{-7} cm^2/s on the air side to 1.1×10^{-6} cm^2/s on the delivery side. A more symmetric profile is observed when a constant value of Do is used. Higher diffusivities are expected on the "fuel" side of the membrane in view of the higher defect concentrations under more reducing chemical potentials. An asymmetric profile is produced with shallower slopes in the profile being seen on the side with higher diffusivity. This shape is accordance with that shown in the data in Figure 20. This general pattern of differentiation was observed in all of the trial simulations, regardless of the degree of reversibility in the surface reactions.

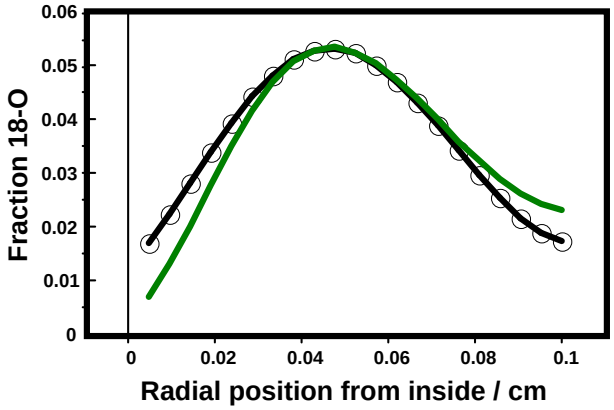

Figure 21. Internal ^{18}O profiles calculated for constant Do (open circles) and Do which increases linearly by a factor of 5 across the membrane (solid line). The air-side surface reaction was assumed to be irreversible.

The gradient in Do is not reliably evident in the isotope transient in the delivery-side gas. Figure 22 shows the isotope transients in the delivery-side gas for the two simulations in Figure 21. The two curves are almost identical while the internal profiles readily reveal the Do variation.

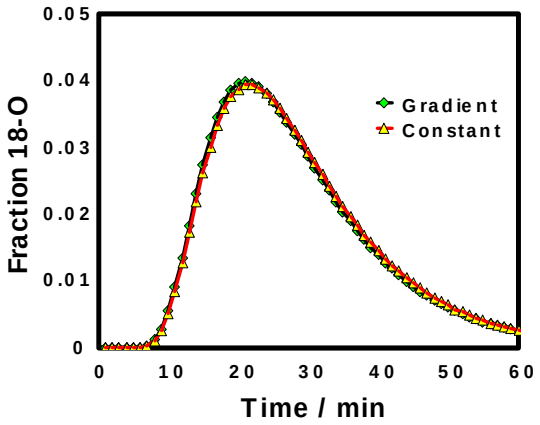

Figure 22. Isotope transients in the delivery-side gas for the case of constant Do (triangles) and for a linear gradient in Do (diamonds). See text for discussion.

The linear parameters above provided the best fit to the experimental data. This fit is shown in Figure 23.

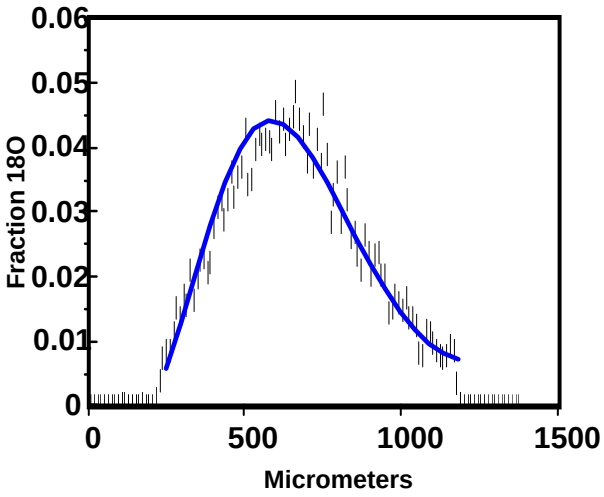

Figure 23. Fit of experimental isotope profile with a linear variation of Do with location in the membrane.

The local value of Do at steady state is governed by the vacancy concentration which is governed by the local chemical (oxygen) potential (in the case of high electronic conductivity). This is not expected to yield a linear variation in Do. We have begun work on a simultaneous defect/transport model which will incorporate the previously measured thermodynamic oxygen stoichiometry data and will report on this in the next quarter.

Surface reaction rates:

In previous reports of the membrane experiments leading up to the quenched profile above, we documented a substantial change in the membrane flux condition which accompanied a relatively small change in the feed gas to the fuel (delivery) side. Upon a switch from 0.1 atm CO + 0.5 atm CO_2 to 0.5 atm CO + 0.1 atm CO_2, the oxygen flux (and the surface rates) increased by a factor of 10. At the first condition, some molecular oxygen was evolved simultaneously with CO oxidation. At the second condition, oxygen evolution ceased. Thus, the more oxidized surface was less active for CO oxidation than the more reduced surface. It is possible that the separation of an iron metal phase mentioned above was involved in this drastic change in kinetics. Since the sample was sacrificed for the profile experiments, we did not examine the reversibility of this seemingly bimodal behavior.

Plans for the next quarter:

Modelling of data: A full defect model will be assembled and checked for consistency with the known thermodynamics of LSCrF. This model will also be applied to our previous experiments on LSCF.

Publications and Presentation:

J. Yoo, A. Verma, S. Wang, A. J. Jacobson, "Oxygen transport kinetics in $SrFeO_{3-x}$, $La_{0.5}Sr_{0.5}FeO_{3-x}$, and $La_{0.2}Sr_{0.8}Cr_{0.2}Fe_{0.8}O_{3-x}$ measured by electrical conductivity relaxation". Journal of the Electrochemical Society (2005), 152(3), A497-A505.

N. Bayani, C.A. Mims, A.J. Jacobson, and P.A.W. van der Heide, "Modes of surface exchange in $La_{0.2}Sr_{0.8}Cr_{0.2}Fe_{0.8}O_{3-d}$" Solid State Ionics (2005) 176(3-4) 319-323.

C. Y. Park and A. J. Jacobson, "Electrical Conductivity and Oxygen Non-stoichiometry of $La_{0.2}Sr_{0.8}Fe_{0.55}Ti_{0.45}O_{3-\delta}$", Journal of the Electrochemical Society (2005) in press.

C. Y. Park and A. J. Jacobson, "Thermal and chemical expansion properties of $La_{0.2}Sr_{0.8}Fe_{0.55}Ti_{0.45}O_{3-x}$" Solid State Ionics accepted.

Three abstracts were accepted at the International Solid State Ionics conference to be held in Baden-Baden Germany July 2005.

CONCLUSIONS

In the current research, the oxygen occupancy was investigated at 1200^{o}C as a function of oxygen activity and compared with that at 1000^{o}C. The cause of bumps at about 200^{o}C was also investigated by using different heating and cooling rates during TGA. The TGA measurements were carried out as a function of temperature in air and as a function of oxygen activity at 1200^{o}C. The bumps were also observed at near 200^{o}C during heating and cooling in air in the current research. To investigate these bumps, weight changes of the bumps were measured at different heating and cooling rates and compared each other.

Fracture toughness of the LSFT and dual phase membranes were calculated using the Vicker's indentation method. The fracture toughness of the LSFT membrane was 1.6 MPa.m$^{1/2}$ and it is slightly higher than the dual phase membrane. The extensive analysis of the crack propagation behavior confirms the toughening mechanisms involved in determining the fracture toughness are grain bridging, crack branching and crack deflection. In the LSFT membrane the grain bridging was found to be the most prominent toughening mechanism among others. This may be due to the intergranular fracture behavior of the membrane. In the case of LSFT-CGO membrane, the prominent toughening mechanism was crack deflection by the dense aggregates.

We have continued to investigate the thermodynamic properties (stability and phase-separation behavior) and total conductivity of prototype membrane materials. The data are needed together with the kinetic information to develop a complete model for the membrane transport. We have previously reported characterization, stoichiometry, conductivity, and dilatometry measurements for samples of $La_{0.2}Sr_{0.8}Fe_{0.55}Ti_{0.45}O_{3-x}$. In this period, we have investigated by transmission electron microscopy the microstructure of ferrites that show very slow kinetics in the intermediate pressure range. The data suggest that the non-equilibrium behavior is associated with the formation of nano-particles of a reduced component which re-react at long times.

In the area of isotope transient studies at steady state, the current quarter has been dominated by continued analysis of the data from the isotope transients and the analysis of the profile in the quenched membrane.

REFERENCES:

1. Evans, A.G., Charles, E. A. (1976), J. Am. Ceram. Soc. 59, 371-372
2. Niihara, K., Morena, R., Hasselman, D.P.H. (1982), J. Mat. Sci. Letters 1, 13-16
3. Antis, G.R., Chantikul, P., Lawn, B.R., Marshall, D.B. (1981), J. Am. Ceram. Soc.64, 533-538.
4. Lawn, B.R., Evans, A.G., Marshall, D.B. (1980), J. Am. Ceram. Soc. 63, 574-581

BIBLIOGRAPHY **N/A**

LIST OF ACRONYMS AND ABBREVIATIONS

YSZ	Yttria stabilized zirconia
XRD	X-ray diffraction
$La_{0.2}Sr_{0.8}Fe_{0.55}Ti_{0.45}O_{3-\delta}$ LSFTO	
IEDP	Isotope exchange and depth profiling
SIMS	Secondary Ion Mass Spectroscopy